Supporting Information

A Free-standing Nanoporous NiCoFeMoMn High Entropy Alloy as An Efficient Electrocatalyst Fast Driving Water Splittling

Hao Liu[1,2,3], *Hongye Qin*[1], *Jianli Kang*[1*], *Liying Ma*[1*], *Guoxin Chen*[3*], *Qin Huang*[4], *Zhijia Zhang*[2], *Enzuo Liu*[1], *Huanming Lu*[3], *Naiqin Zhao*[1]

[1]School of Materials Science and Engineering, Tianjin University, Tianjin 300350, China

[2]School of Materials Science and Engineering, Tiangong University, Tianjin 300387, China

[3]Ningbo Institute of Materials Technology & Engineering, Chinese Academy of Sciences, Ningbo 315201, China.

[4]Guangdong Institute of Semiconductor Industrial Technology, Guangdong Academy of Sciences, Guangzhou 510651, China

*Corresponding author. E-mail: jianlikang@tju.edu.cn (J. Kang); lyma@tju.edu.cn (L.-Y. Ma); gxchen@nimte.ac.cn (G. Chen)

1.1 Synthesis of the precursor high entropy NiCoFeMoMn ribbons.

The high entropy alloy with theoretical atomic ratio of $Ni_{14}Co_{14}Fe_{14}Mo_6Mn_{52}$ was prepared by mixing the metal particles of nickel (Ni), cobalt (Co), iron (Fe), molybdenum (Mo) and manganese (Mn) with purity higher than 99.9%. The precursor high entropy NiCoFeMoMn alloy ribbons was prepared by arc melting and single-roller melt spinning. In order to ensure that the components of the prepared high entropy alloy are more uniform, Firstly, NiCoFeMo was prepared into alloy ingot by arc melting under a Ti-gettered argon atmosphere in a water-cooled copper crucible. After that, the prepared NiCoFeMo alloy ingot and metal Mn are prepared to form the precursor high entropy NiCoFeMoMn ribbons by single-roller melt spinning. When the material passes through the cold surface of the copper roller, it will be rapidly quenching to room temperature to form a face centered cubic (FCC) high entropy alloy ribbons with the size of 25μm thick and ~2mm wide. The precursor high entropy NiCoFeMoMn ribbons are cut into a thin sheet metal with the size of 1cm length and 0.2cm wide for preparation of nanoporous-NiCoFeMoMn high entropy alloy catalyst.

2.2 Synthesis of the nanoporous-NiCoFeMoMn catalyst.

The np-NiCoFeMoMn catalyst was fabricated by a facile one step electrochemistry dealloying process in the 1.0 M $(NH_4)_2SO_4$ (Shanghai Macklin Biochemical Co., Ltd) solution using an electrochemical workstation (CHI 760) in a standard three electrode system with a graphite rod as the counter electrode and Ag/AgCl electrode as reference electrode. Under the voltage of - 0.5V (vs Ag/AgCl), different surface morphology and atomic proportion can be obtained by controlling different corrosion time intervals of 2, 3, 4, 5 and 6h to remove metal components. The dealloyed high entropy alloys were rinsed at least three times with deionized water to eliminate residual chemical reagent before storing in anhydrous ethanol until electrochemical testing is performed.

2.3 Materials characterization

A Bruker D8 Advance Davinci X-ray diffraction (XRD) instrument was employed by *Cu-K*α radiation with a monochromator to identify the FCC-phase structure of the

HEA and the structural evolution during the dealloying process. The diffraction patterns were recorded by continued scanning in the 2θ range of 20°–100°. Zeiss Auriga is used to show the surface morphology and element composition with energy-dispersive X-ray spectroscopy (EDS). Transmission electron microscopy (TEM) images were taken on an FEI TF20 field-emission transmission electron microscope operating at 200 kV, selected area electron diffraction (SAED), high-resolution transmission electron microscopy (HR-TEM) images, scanning transmission electron microscopy (STEM) images and energy-dispersive X-ray spectroscopy images are also obtained by this device. The TEM specimens was prepared on using a Zeiss focused ion beam/scanning electron microscope (FIB/SEM). The surface characteristics of the samples were investigated using Kratos Axis Ultra DLD X-ray photoelectron spectrometer (XPS). The specific surface area and pore size distribution were determined by nitrogen adsorption-desorption tests using the BET. The contact angles of droplets on the sample surfaces were recorded by Dataphysics OCA20.

2.4 Electrochemical measurements.

The catalyst of electrochemical measurements throughout in this work was tested in 1.0 M KOH (Shanghai Wokai Biochemical Co., Ltd) solutions using an electrochemical workstation (CHI 760) in a standard three electrode system with a graphite rod or Pt sheet as the counter electrode and Ag/AgCl electrode as reference electrode, respectively. The Ag/AgCl electrode was rinsed with deionized water before use. All the potential in this work are calibrated by reversible hydrogen electrode (E vs. RHE) on the basis of the Nernst equation with iR compensation. The dealloyed np- NiCoFeMoMn high entropy alloy and a Pt sheet are directly used as the working electrodes. The current density was Calculated by the geometric area of the specimens. Linear sweep voltammetry (LSV) was tested with a scan rate of 1 mV s^{-1}. Electrochemical impedance spectroscopy (EIS) was carried out from 0.01 to 10^5 Hz. A series of cyclic voltammetries (CVs) were carried out at sweep rates of 5 - 100 mV s^{-1} at non-faradaic overpotentials to demonstrate the current charging and discharging capacitance for estimating the double-layer capacitance (C_{dl}). The electrochemical surface area (ECSA) value was obtained according to the equation of ECSA = C_{dl}/C_s, where C_{dl} is the measured double-layer capacitance and C_s is the specific capacitance. In this work, we assumed the C_s value at 40 μF cm^{-2} due to the flat surface of the HEAs. The stability measurement was carried out at a static current density of 100 and 500 mA cm^{-2} by a chronoamperometry method without iR compensation. For the electrochemical test, the catalysts inks (5 mg mL^{-1} for Pt/C) were prepared by dispersing the catalyst in a mixture of water and isopropyl alcohol at volume ratio of 5:5 with 0.05wt% Nafion as a binder by sonicating for 30 min to get a uniform suspension. An aliquot of 8 μL of Pt/C was deposited on the polished 5 mm glassy carbon electrode.

2.5 Calculation of price activity

In order to compare price activities of Pt/C and np-NiCoFeMoMn 6h, their mass activity was calculated first. The overpotential of -100 mV was selected to evaluate the mass activity and price activity. The details are as follows:

$$\mathrm{j}_{\mathrm{mass}}^{\mathrm{Pt/C}} = \frac{j_{area}^{Pt/C}(mA/cm^2)}{mass_{Pt}} = \frac{31.47(mA/cm^2)}{0.2(mg/\mathrm{cm}^2)} = 157.35A/g$$

$$\mathrm{j}_{\mathrm{mass}}^{np-HEA} = \frac{j_{area}^{np-HEA}}{mass_{np-HEA}} = \frac{463.87(mA/cm^2)}{6.81(mg/cm^2)} = 68.12A/g$$

$$\mathrm{j}_{\mathrm{price}}^{Pt/C} = \frac{mass-activity_{Pt/C}}{price_{Pt/C}} = \frac{157.35(A/g)}{974/28.3495(dollar/g)} = 4.6(A/dollar)$$

$$\mathrm{j}_{\mathrm{price}}^{np-HEA} = \frac{mass-activity_{np-HEA}}{price_{np-HEA}} = \frac{68.12(A/g)}{0.0187(dollar/g)} = 3642.8(A/dollar)$$

2.6 Model Confirmation

The special quasi-random structure method using a Monte Carlo algorithm implemented in ATAT software is employed to model the segregation area ($Mn_{0.4}Fe_{0.15}Co_{0.15}Ni_{0.15}Mo_{0.15}$) and uniform area ($Mn_{0.2}Fe_{0.1}Co_{0.1}Ni_{0.3}Mo_{0.3}$) alloy supercells[1-3], as well as keep the same chemical atomic ratio both in bulk and on surface. Pair correlation functions up to the third nearest neighbors were optimized where the maximum mismatch between the special quasi-random structure and the ideal target alloy was below 0.04. The longest distance when calculating the correlation functions is set as 1.2. After MCSQS optimization, the software generated 16 and 19 geometric structures for segregation area (Mn0.4Fe0.15Co0.15Ni0.15Mo0.15) and uniform area (Mn0.2Fe0.1Co0.1Ni0.3Mo0.3) respectively. We chose the structure with best lower objective function as our supercell model. The slab models are built with vacuum added in the 111 direction.

2.7 Parameter Determination

At least six volumes are used to to the 4-parameter Birch-Murnaghan equation of states (EOS) fitting to obtain equilibrium properties[4]. The optimized lattice parameters for bulk segregation area and and uniform area unit cell parameters were 3.625 and 3.695 Å, respectively, in agreement with experimental XRD values of   Å.

2.8 DFT Caculation

All spin poloried DFT calculations were performed using the projected augmented wave pseudopotentials[5, 6] and Perdew-Burke-Ernzerh of generalized gradient exchange approximation correlational functional as implemented in computational package VASP [7, 8]. The kinetic energy cutoff was set to 600 eV for the plane-wave basis set and the DFT dispersion correction (DFT-D3) method was used to treat the van der Waals interactions[9]. Brillouin zone integration was sampled with the gamma centred 2 × 4 × 1 and 3 × 3 × 1 MonkhorstPack mesh k-point for segregation and uniform surface calculations[10]. The force and energy convergence criteria were set to 0.02 eV $Å^{-1}$ and 10^{-6} eV, respectively. The water adsorption energies (E_{H2O}) at HEA surfaces were calculated by the equation of $EH2O=Esurf+H2O-Esurf-EH2O$, where the $Esurf$ and the $Esurf+H2O$ are the total energies of the surface before and after water adsorption, and $EH2O$is the energy of a free water molecule

In order to understand the catalytic performance for HER, the H adsorption free energy under standard conditions (pH = 0, p(H2) = 1 bar) was computed. The hydrogen adsorption Gibbs free energy ΔG_H is defined as $\Delta G_H = \Delta E_H + \Delta E_{ZPE} - T\Delta S_H$. where ΔE_H is the differential hydrogen adsorption energy, ΔE_{ZPE} is the difference between the zero-point energy of the hydrogen adsorbed state and the gas phase H2. Since the vibrational entropy contribution of the hydrogen adsorbed state is very small, where $S_{H_2}^{\mathrm{O}}$ is the entropy of H2 in the gas phase at the standard conditions. Therefore, the overall contribution can be rewritten as $\Delta G_H = \Delta E_H + 0.24$ $\Delta S_H \approx -\frac{1}{2} S_{H_2}^{\mathrm{O}}$ at room temperature[11].

2.9 Formation mechanism of morphology after dealloyed

We think that the change may be due to the different composition between SA and un-SA, which leads to different open circuit voltage. In order to verify this hypothesis, we prepared two ribbons according to the composition of SA and un-SA, respectively. The open circuit voltages of the two ribbons were measured by CHI760E electrochemical workstation, the value of un-SA and SA are -0.58 and -0.49V (vs Ag/AgCl). Therefore, when electrochemical dealloying is performed at - 0.5V (vs Ag/AgCl), SA will not be dealloyed. At the same time, it forms larger pores due to the corrosion of un-SA area near SA area is more serious.

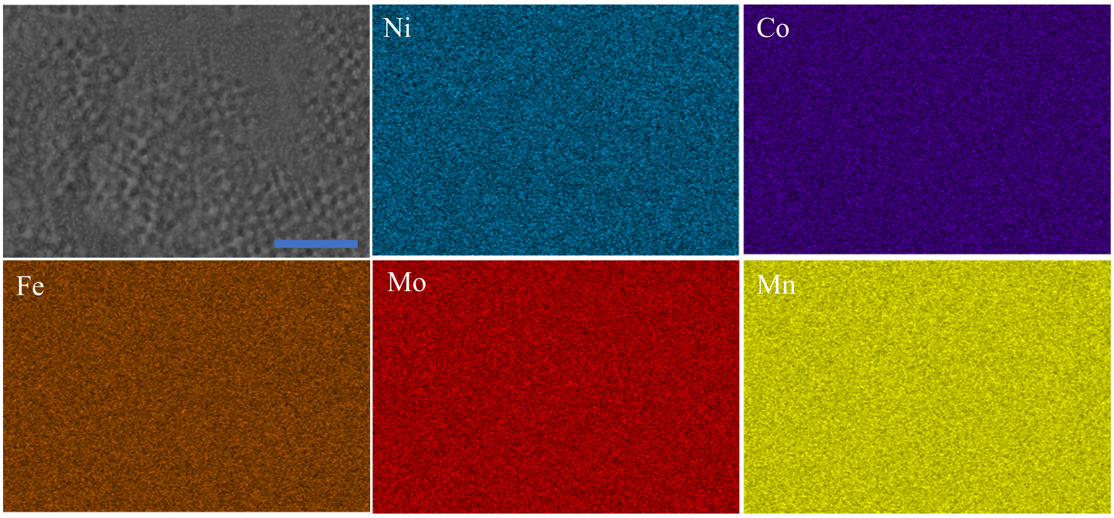

Fig. S1 SEM-EDS of NiCoFeMoMn alloy. Scale bars: 5μm.

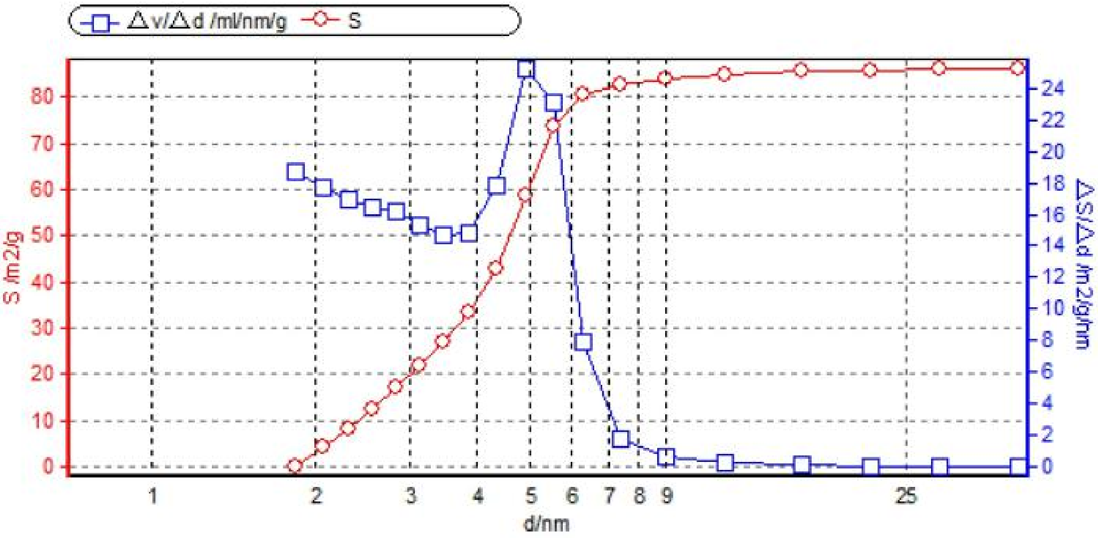

Fig. S2 BET analysis of the nanoporous NiCoFeMoMn electrode was prepared by dealloying in 1M $(NH_4)_2SO_4$.

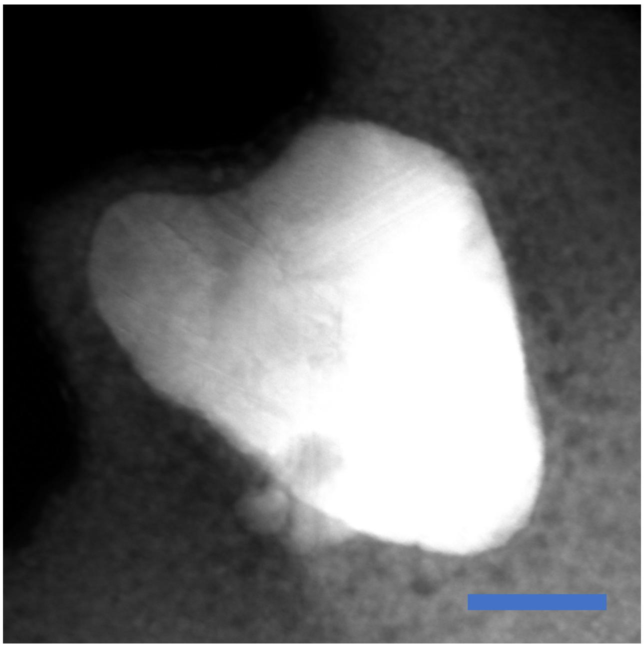

Fig. S3 HADDF-STEM image of NiCoFeMoMn alloy. Scale bars: 50nm.

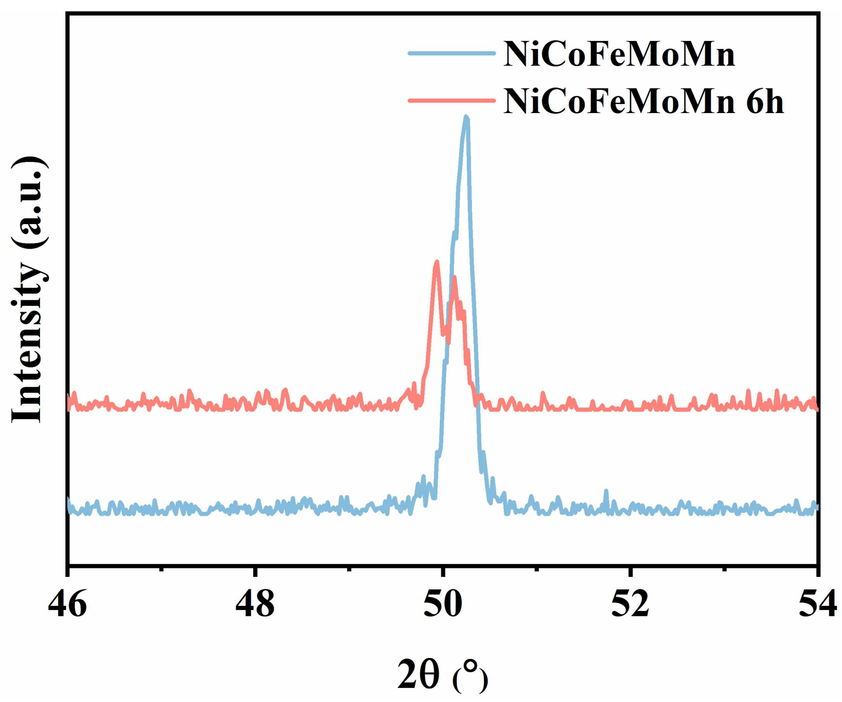

Fig. S4 XRD analysis of the master NiCoFeMoMn alloy and np- NiCoFeMoMn alloy of (200) plane.

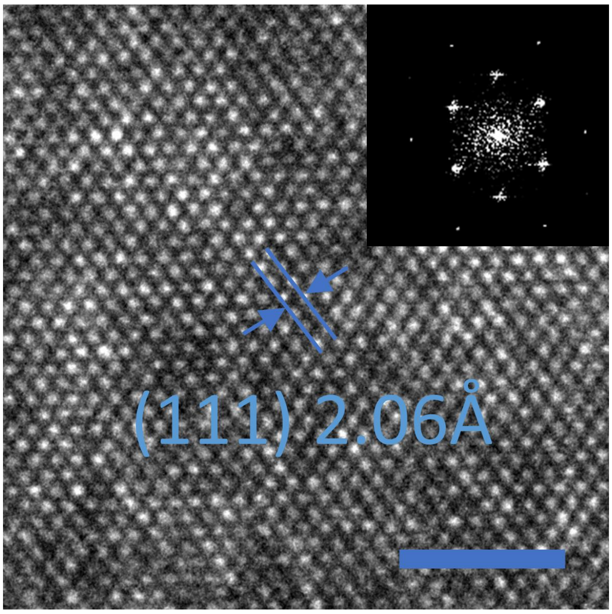

Fig. S5 HR-TEM of NiCoFeMoMn alloy. bar: 2nm

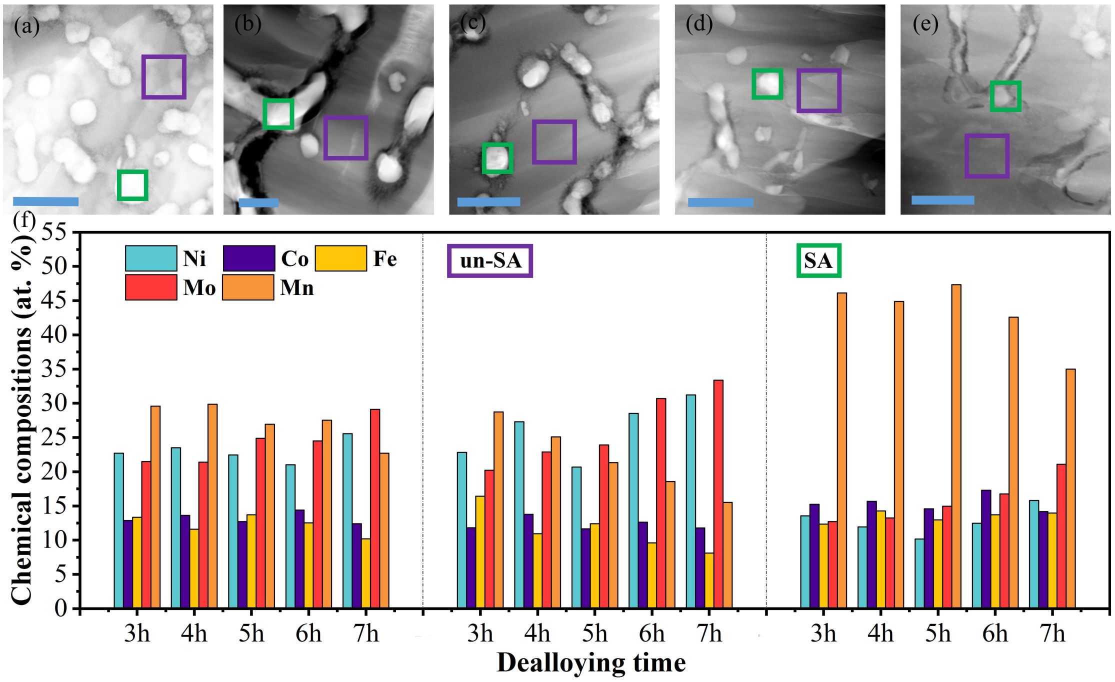

Fig. S6. HADDF-STEM images of np-NiCoFeMoMn with different dealloying time. (a)- (e) 3-7h.(The green box and red box represents the SA and un-SA, respectively. (f) chemical composition of total content, un-SA and SA with different dealloying time. bar: 500nm.

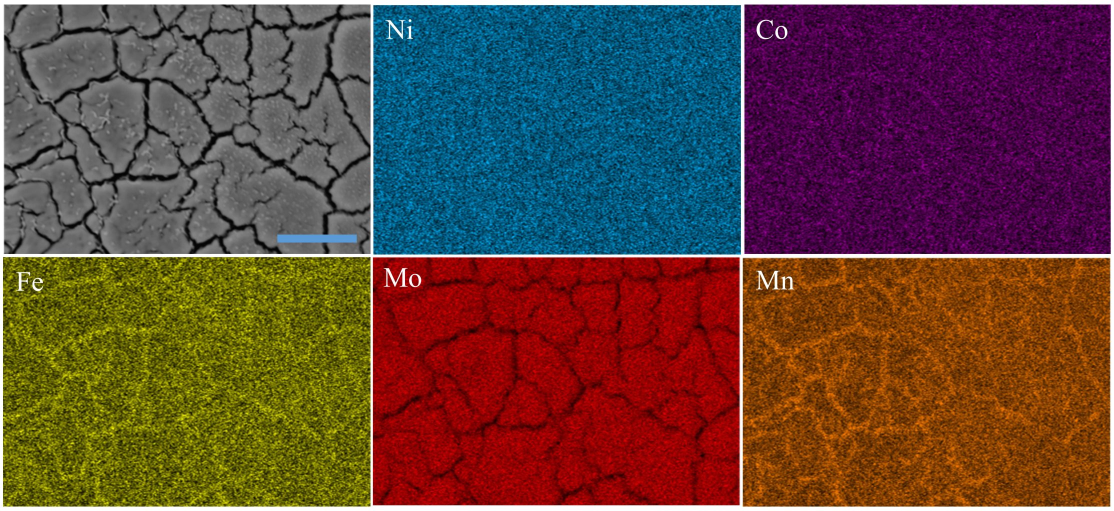

Fig. S7 SEM and EDS of np-NiCoFeMoMn 6h. Scale bars: 10μm.

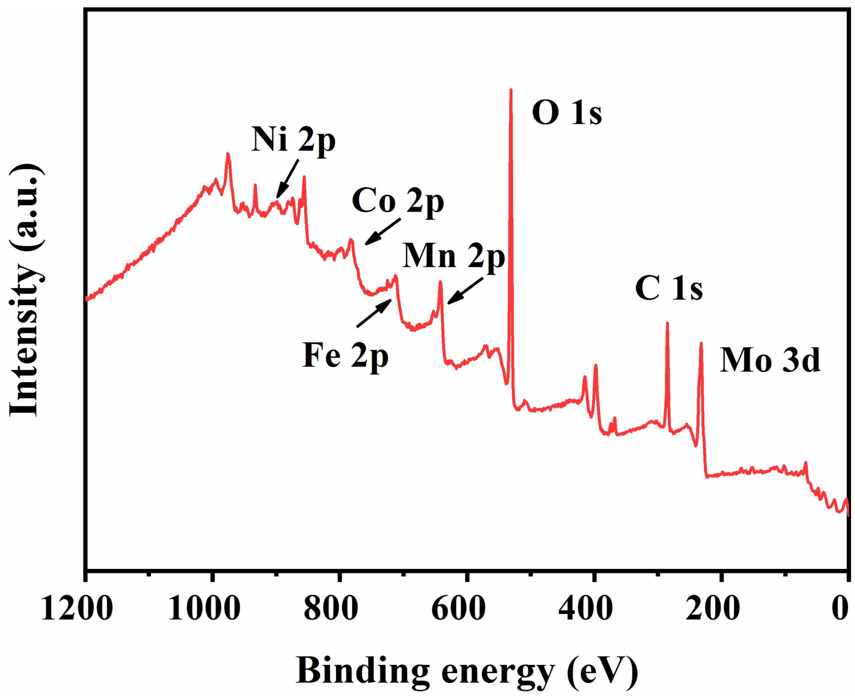

Fig. S8 XPS spectra of np-NiMnFeMo 6h.

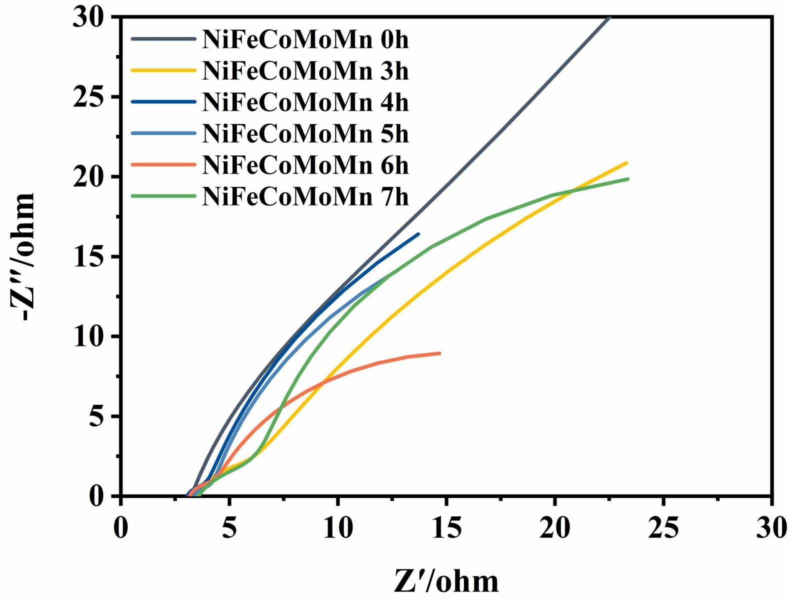

Fig. S9. Electrochemical impedance spectra of np-NiCoFeMoMn under different dealloying time.

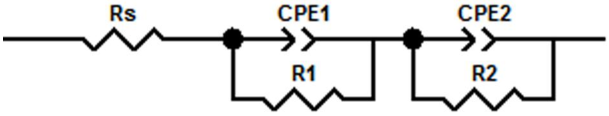

Fig. S10 The np-NiCoFeMoMn 6h’s EIS equivalent circuit diagram in 1M KOH.

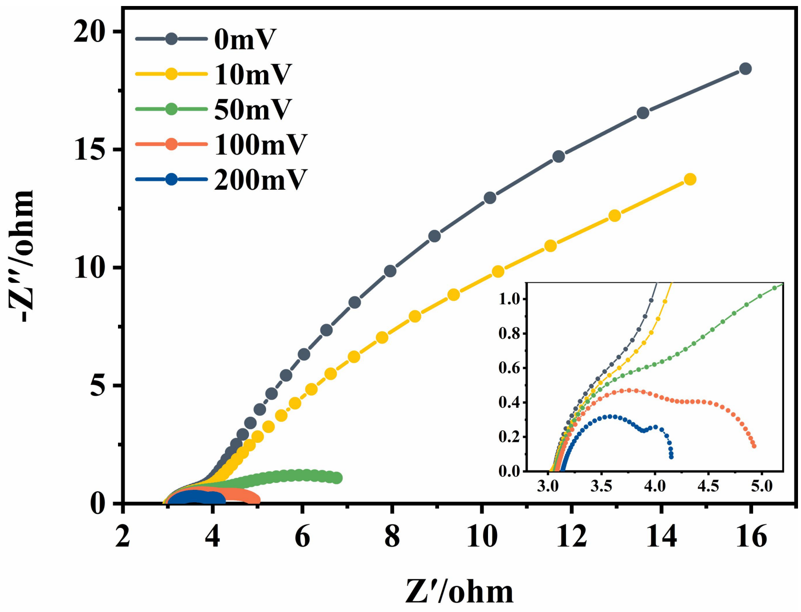

Fig. S11 Electrochemical impedance spectra of np-NiCoFeMoMn 6h under different overpotentials.

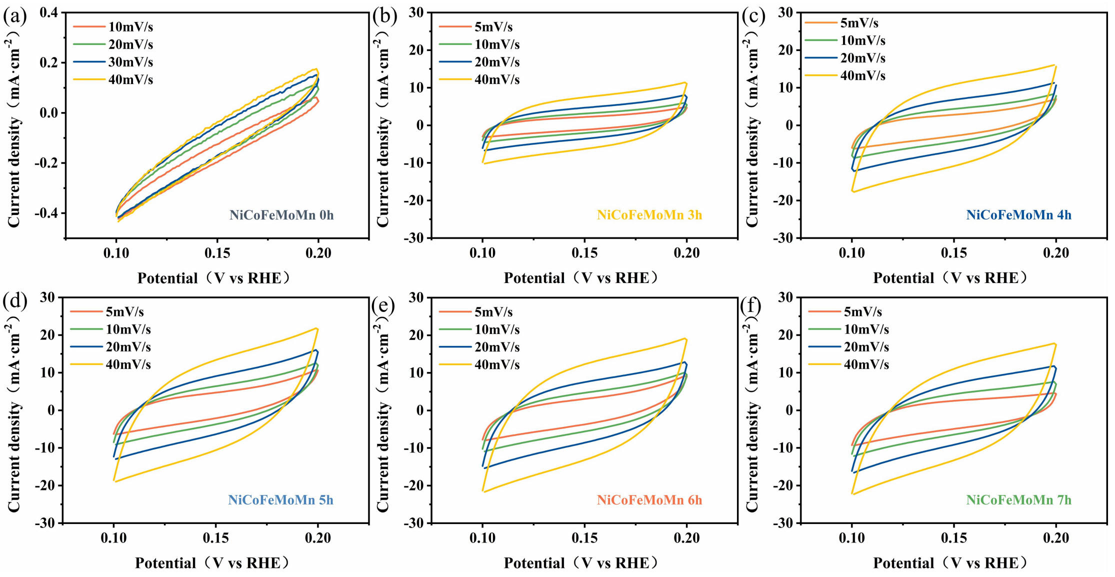

Fig. S12 The double-layer capacitance curve of the nano porous high entropy electrode with different dealloying time.

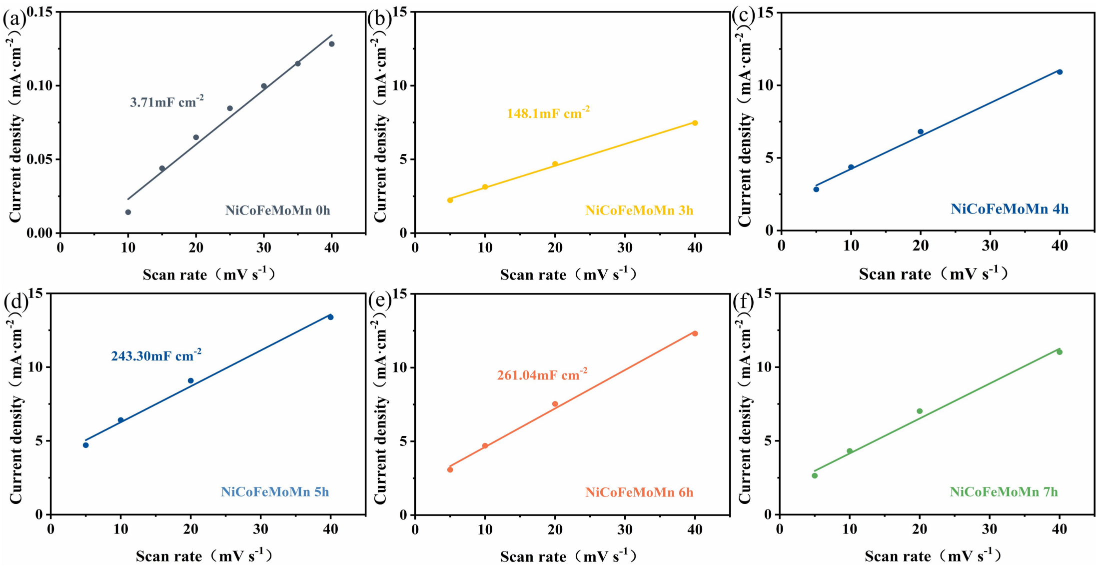

Fig. S13 The capacitive currents plotted against the scan rate at 0.15 V versus RHE for the NiCoFeMoMn alloy and np-NiCoFeMoMn alloy, indicating the benefit of the enlarged surface area of the np-NiCoFeMoMn 6h for the potential electrochemical applications.

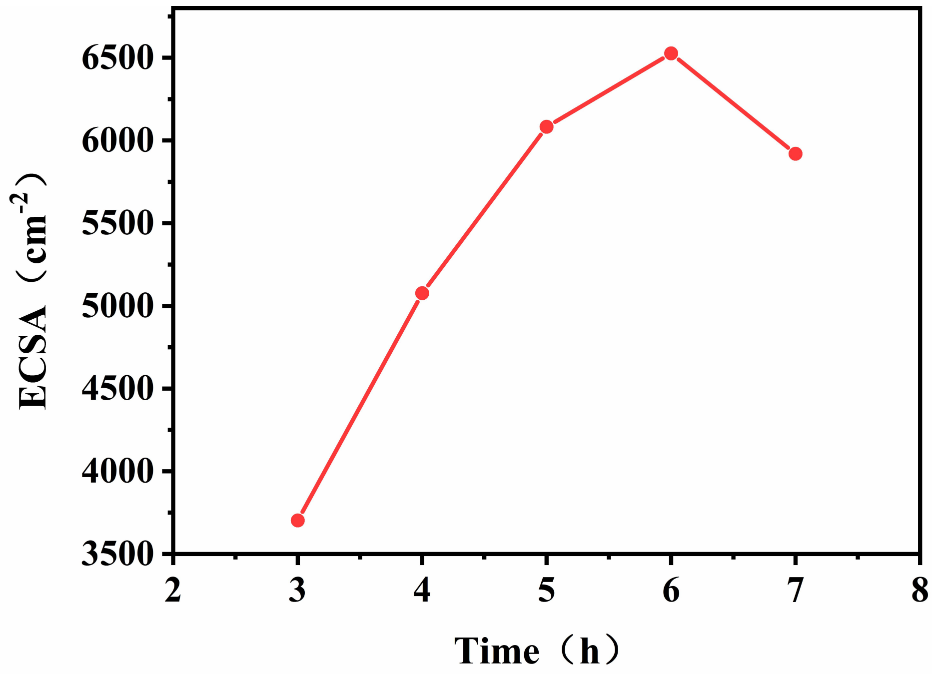

Fig. S14. The dependence of ECSA on the NiCoFeMoMn at different dealloying time intervals, showing the improved active sites during the dealloying process.

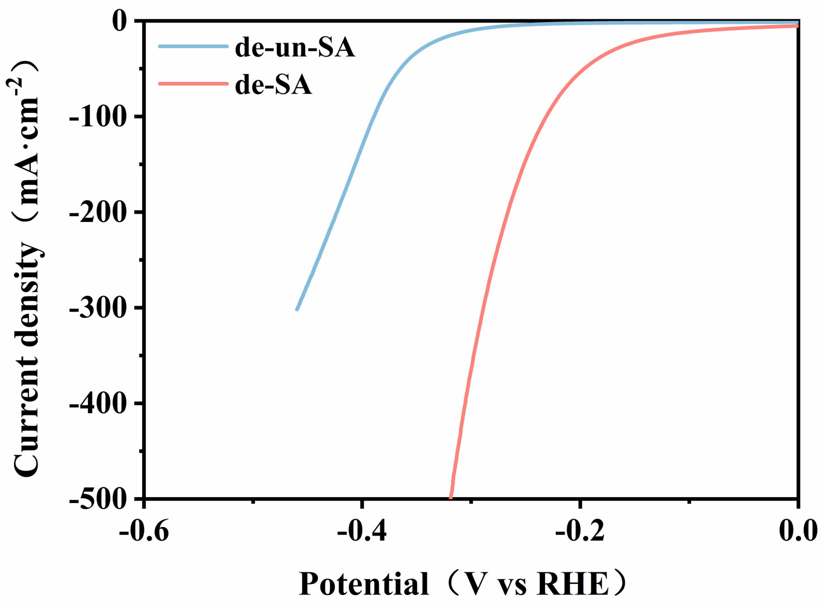

Fig. S15 HER polarization curves for NiCoFeMoMn de-SA and de-un-SA in 1 M KOH solution. Scan rate: 5 mV s^{-1}.

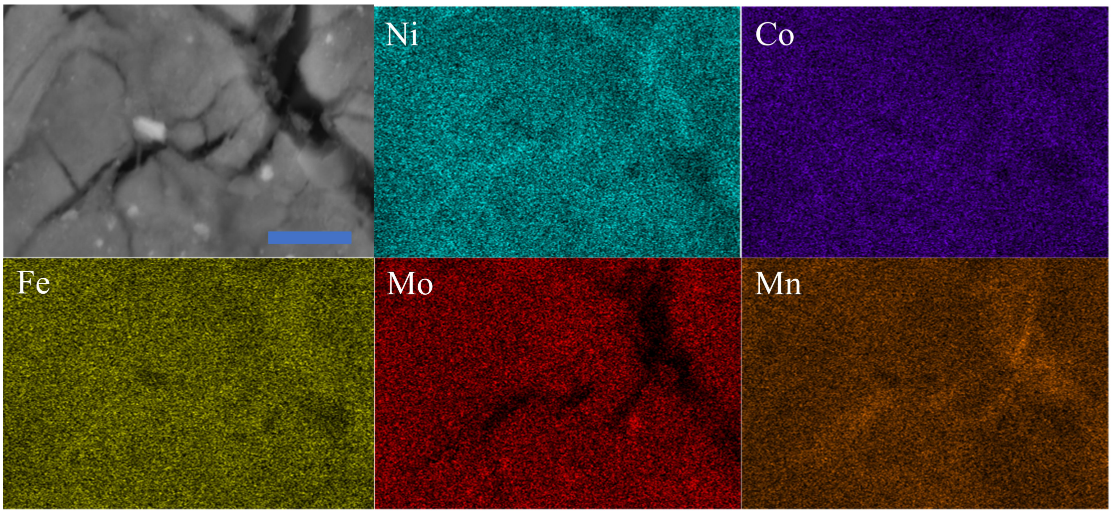

Fig. S16 SEM and EDS of np-NiCoFeMoMn 6h after HER durability test. Scale bars: 2.5μm.

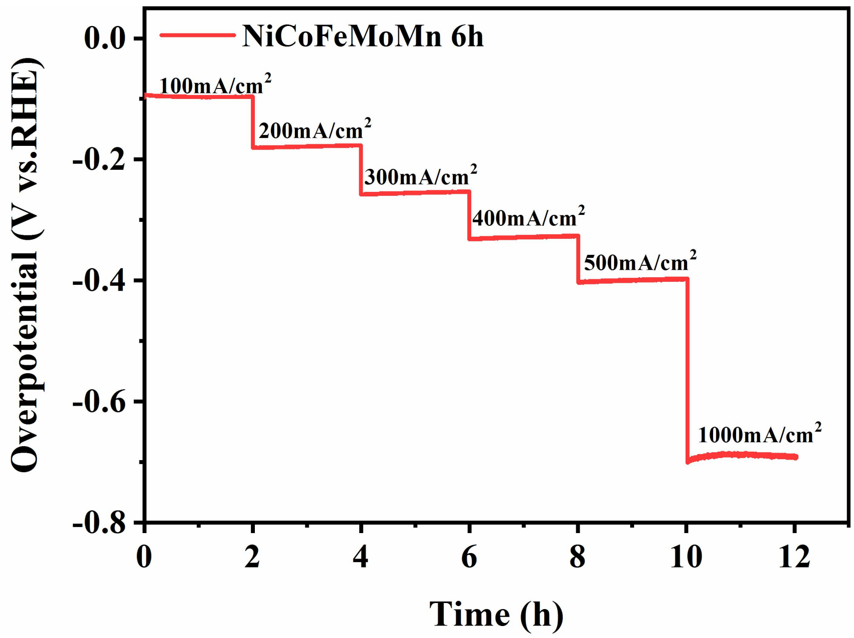

Fig. S17. Multi-step chronoamperometric curve obtained with np-NiCoFeMoMn 6h in 1M KOH, measured at different overpotentials, strating at 0 mV and ending at 690 mV with an increment of 80 or 300 mV every 2 h. (Without iR compensation).

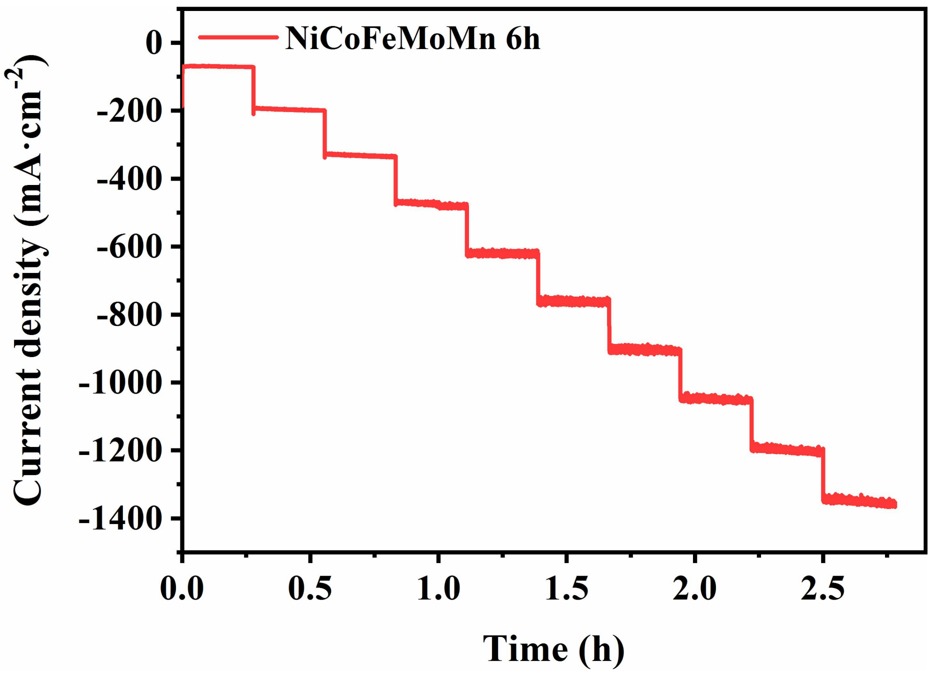

Fig. S18 Multi-step voltage curve obtained with np-NiCoFeMoMn 6h in 1M KOH, measured at different current. (Without iR compensation).

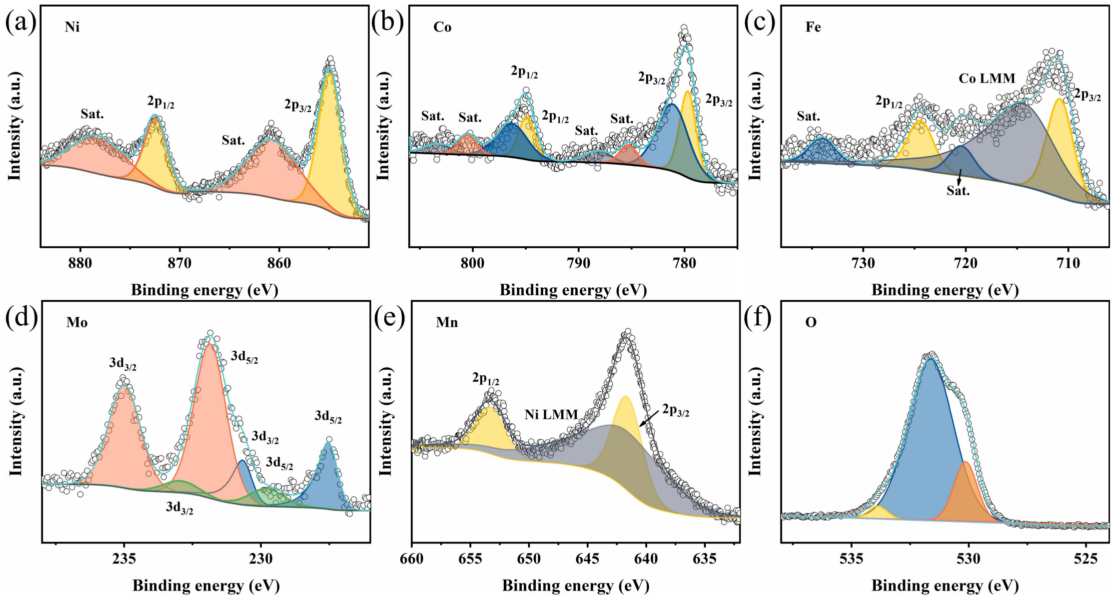

Fig. S19 XPS of polarized np-HEA 6h.

As shown in Fig. S20a shows deconvolution of the Ni 2p core level spectra, which exhibits a pair peak of binding energies of 854.89 and 872.38 eV assigned to metallic Ni(Ⅲ). The indicates that the valence of metal increases after electrochemical oxidation, which is also obvious in other metal elements. In Co 2p region(Fig. S20b), Co(Ⅱ) is the main valence state, and its peak at 781.10 eV (2p3/2) and 796.30 eV (2p1/2); the peaks of Co(Ⅲ) at 779.68 (2p3/2) and 794.88 eV (2p1/2); The Fe 2p spectrum in Fig. S20c shows a pair peak at 710.82 and 724.42 eV, which can be ascribed to Fe 2p 3/2 and Fe 2p 1/2 of Fe(Ⅱ), respectively. The peak-fitting analysis Mo 3d spectrum (Fig. S20d) shows that all metallic Mo, Mo(Ⅳ) and Mo(Ⅵ). From the Mn 2p spectrum (Fig. S20e), that the peak of 641.59 and 653.29 eV can be assigned to Mn 2p 3/2 and Mn 2p 1/2 of Mn(Ⅲ); The O 1s XPS spectrum in Fig. S20f can be simulated by the combination of three features at 530.14, 531.63 and 533.87eV, corresponding to the M-O, M-OH and H_2O on surface of polarized np-HEA 6h. The M-OH content of the polarized np-HEA is much higher than that of the np-HEA.

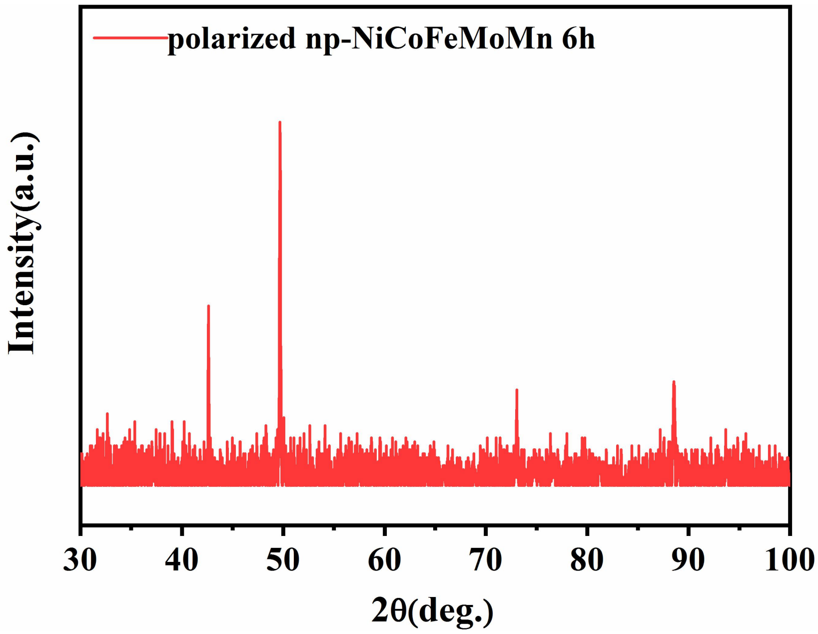

Fig. S20 XRD analysis of the polarized np-HEA 6h.

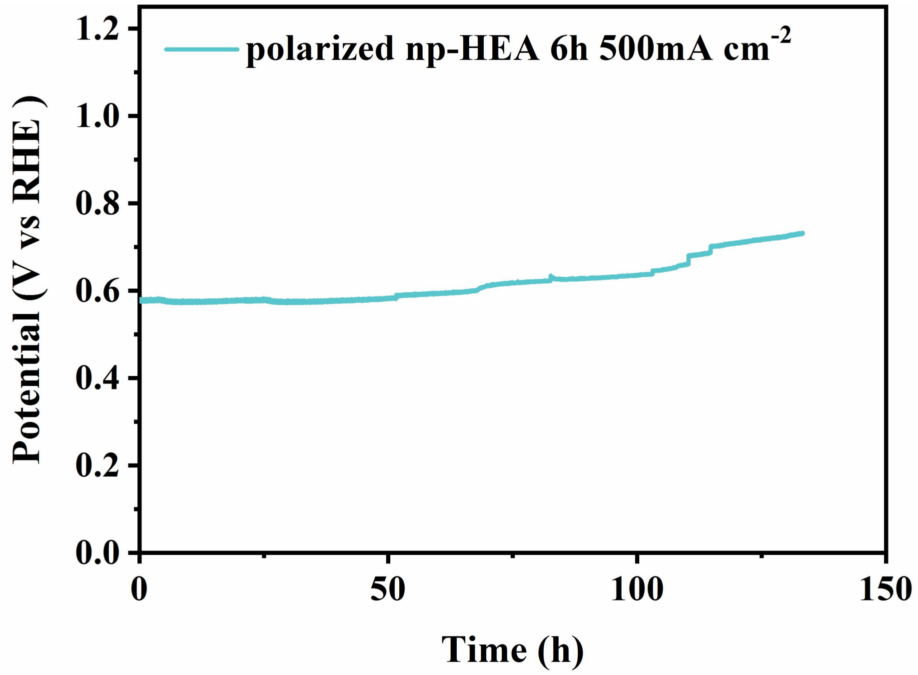

Fig. **S**21 The time-current curves of the polarized np-HEA 6h at a current density of 500 mA cm^{-2} without iR.

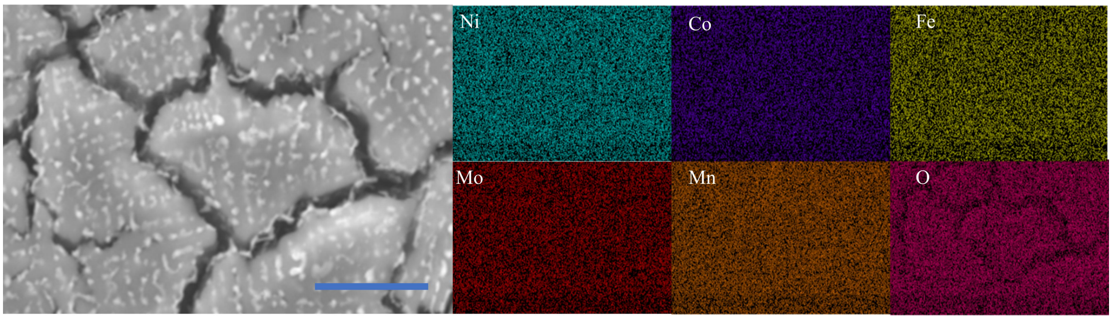

Fig. S22 SEM and EDS of polarized np-HEA 6h after OER durability test. Scale bars: 5μm.

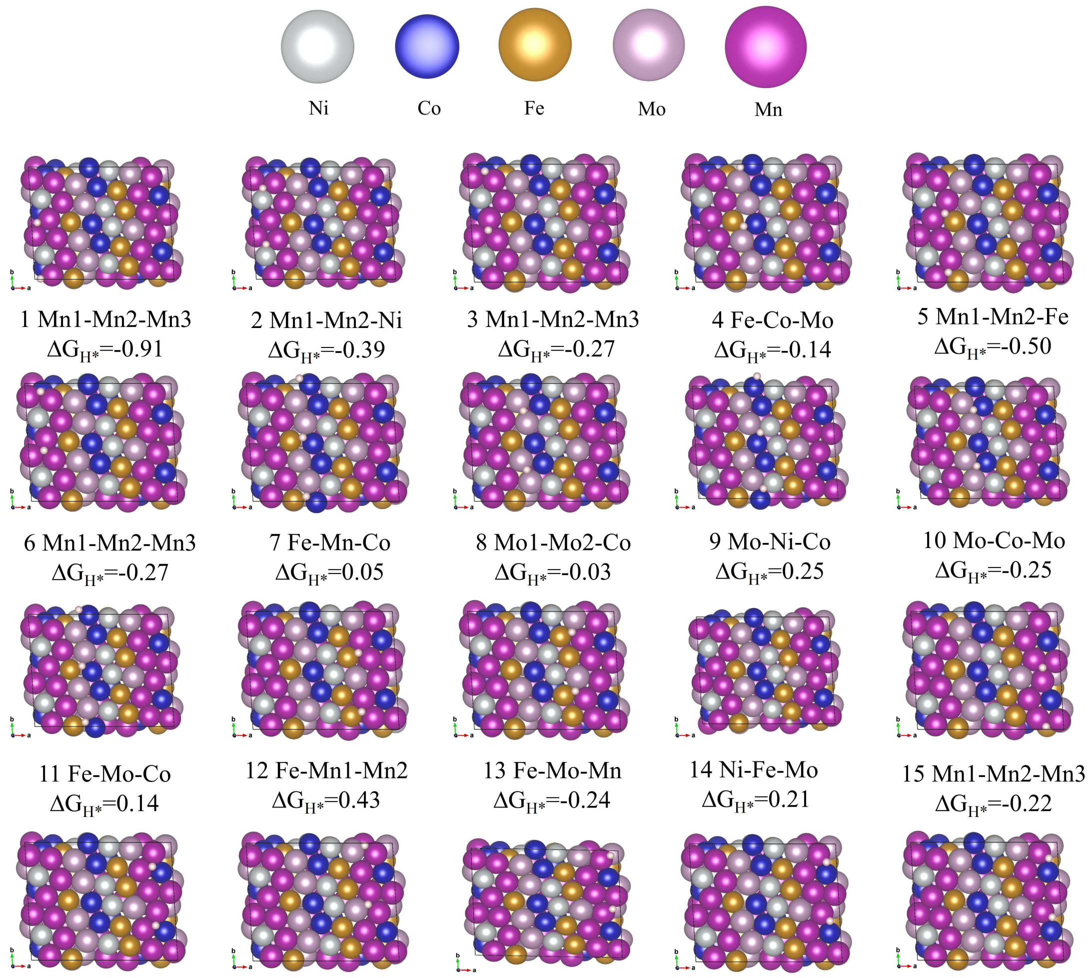

1 Mn1-Mn2-Mn3 ΔG_{H*}=-0.91

2 Mn1-Mn2-Ni ΔG_{H*}=-0.39

3 Mn1-Mn2-Mn3 ΔG_{H*}=-0.27

4 Fe-Co-Mo ΔG_{H*}=-0.14

5 Mn1-Mn2-Fe ΔG_{H*}=-0.50

6 Mn1-Mn2-Mn3 ΔG_{H*}=-0.27

7 Fe-Mn-Co ΔG_{H*}=0.05

8 Mo1-Mo2-Co ΔG_{H*}=-0.03

9 Mo-Ni-Co ΔG_{H*}=0.25

10 Mo-Co-Mo ΔG_{H*}=-0.25

11 Fe-Mo-Co ΔG_{H*}=0.14

12 Fe-Mn1-Mn2 ΔG_{H*}=0.43

13 Fe-Mo-Mn ΔG_{H*}=-0.24

14 Ni-Fe-Mo ΔG_{H*}=0.21

15 Mn1-Mn2-Mn3 ΔG_{H*}=-0.22

16 Mn1-Mn2-Co ΔG_{H*}=0.01

17 Mo-Mn1-Mn2 ΔG_{H*}=-0.65

18 Mn1-Mn2-Mn3 ΔG_{H*}=-0.02

19 Mn1-Mn2-Co ΔG_{H*}=-0.25

20 Mn1-Mn2-Co ΔG_{H*}=-0.25

Fig. S23 Local chemical environment of H_{ad} adsorption sites at HEA-(111) (SA) surfaces with various ΔG_{H*}.

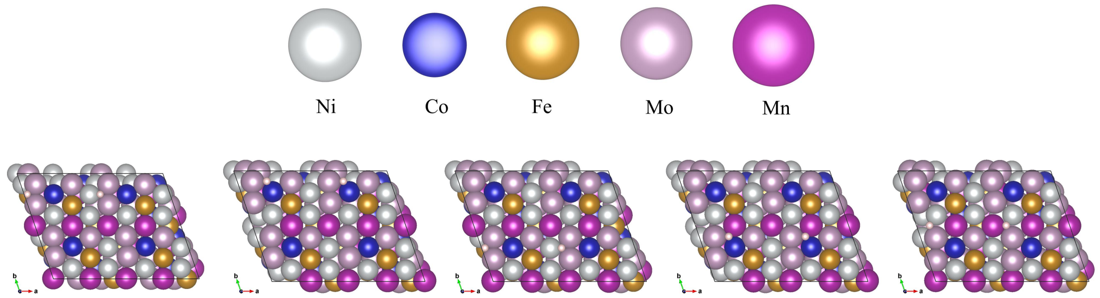

1 Ni1-Mo1-Mo2 ΔG_{H*}=-0.56

2 Mo-Mn-Co ΔG_{H*}=-0.63

3 Ni2-Mo1-Mo2 ΔG_{H*}=-0.56

4 Mo-Mn-Co ΔG_{H*}=-0.63

5 Mn-Ni-Co ΔG_{H*}= 0.30

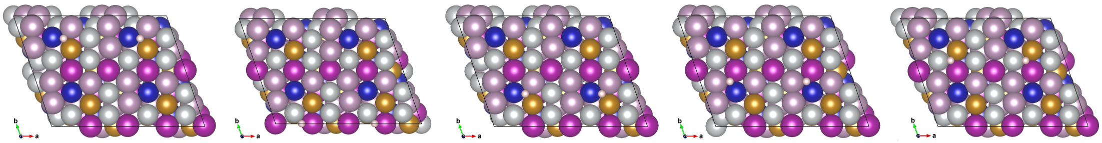

6 Co-Mo-Fe ΔG_{H*}=-0.58

7 Mo-Ni-Mn ΔG_{H*}=1.55

8 Co-Mo-Fe ΔG_{H*}=-0.58

9 Mo-Mn-Co ΔG_{H*}=-0.63

10 Ni-Fe-Mn ΔG_{H*}=-0.36

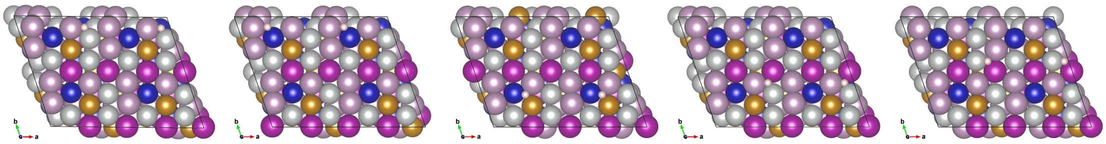

11 Mo-Mn-Ni ΔG_{H*}=-0.57

12 Mo-Mn-Co ΔG_{H*}=-0.63

13 Co-Mo-Fe ΔG_{H*}=-0.59

14 Mo-Mn-Ni ΔG_{H*}=-0.57

15 Ni-Mo-Mn ΔG_{H*}=-0.54

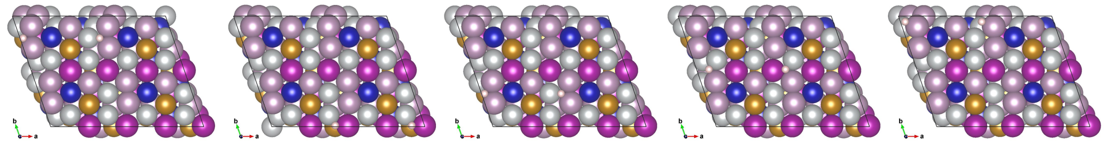

16 Ni1-Mo1-Mo2 ΔG_{H*}=-0.61

17 Mo-Ni-Mn ΔG_{H*}=-0.57

18 Ni2-Mo2-Mo2 ΔG_{H*}=-0.51

19 Mn-Ni-Mo ΔG_{H*}=-0.51

20 Ni-Mn-Mo ΔG_{H*}=-0.41

Fig. S24 Local chemical environment of H_{ad} adsorption sites at HEA-(111) (un-SA) surfaces with various ΔG_{H*}.

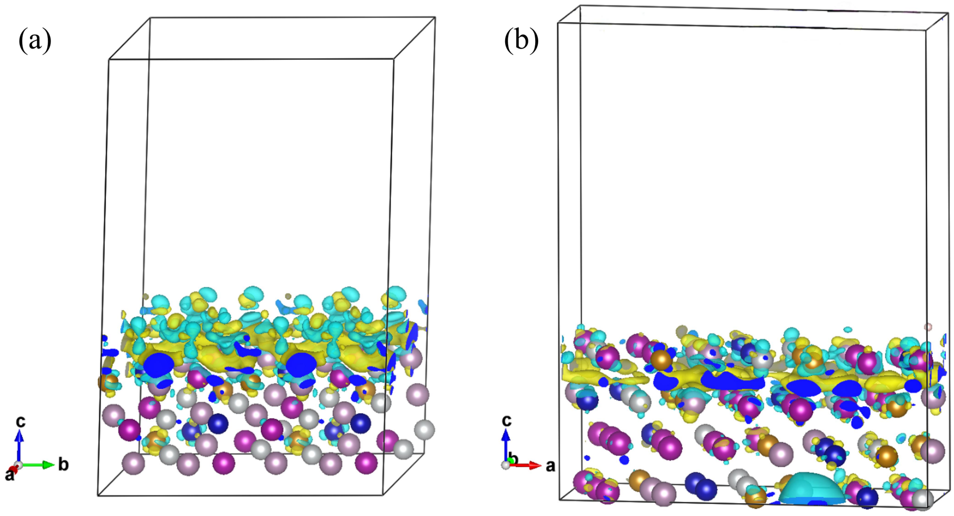

Fig. S25 three-dimensional charge density difference of surface with isosurface value of 0.07e/Bohr^3. (a) un-SA. (b) SA.

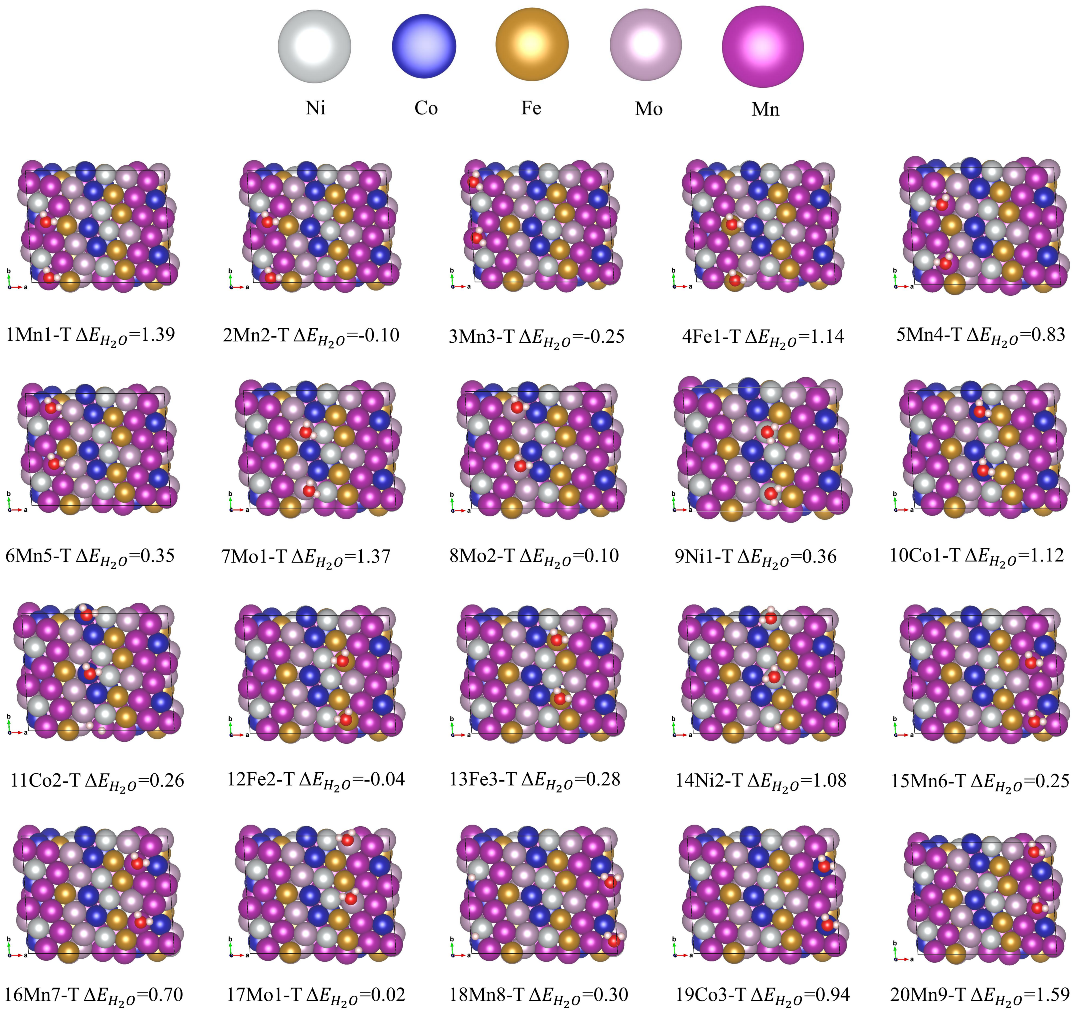

1Mn1-T ΔE_{H_2O}=1.39 2Mn2-T ΔE_{H_2O}=-0.10 3Mn3-T ΔE_{H_2O}=-0.25 4Fe1-T ΔE_{H_2O}=1.14 5Mn4-T ΔE_{H_2O}=0.83

6Mn5-T ΔE_{H_2O}=0.35 7Mo1-T ΔE_{H_2O}=1.37 8Mo2-T ΔE_{H_2O}=0.10 9Ni1-T ΔE_{H_2O}=0.36 10Co1-T ΔE_{H_2O}=1.12

11Co2-T ΔE_{H_2O}=0.26 12Fe2-T ΔE_{H_2O}=-0.04 13Fe3-T ΔE_{H_2O}=0.28 14Ni2-T ΔE_{H_2O}=1.08 15Mn6-T ΔE_{H_2O}=0.25

16Mn7-T ΔE_{H_2O}=0.70 17Mo1-T ΔE_{H_2O}=0.02 18Mn8-T ΔE_{H_2O}=0.30 19Co3-T ΔE_{H_2O}=0.94 20Mn9-T ΔE_{H_2O}=1.59

Fig. S26 Local chemical environment of H_2O adsorption sites at HEA-(111) (SA) surfaces with various *ΔG*.

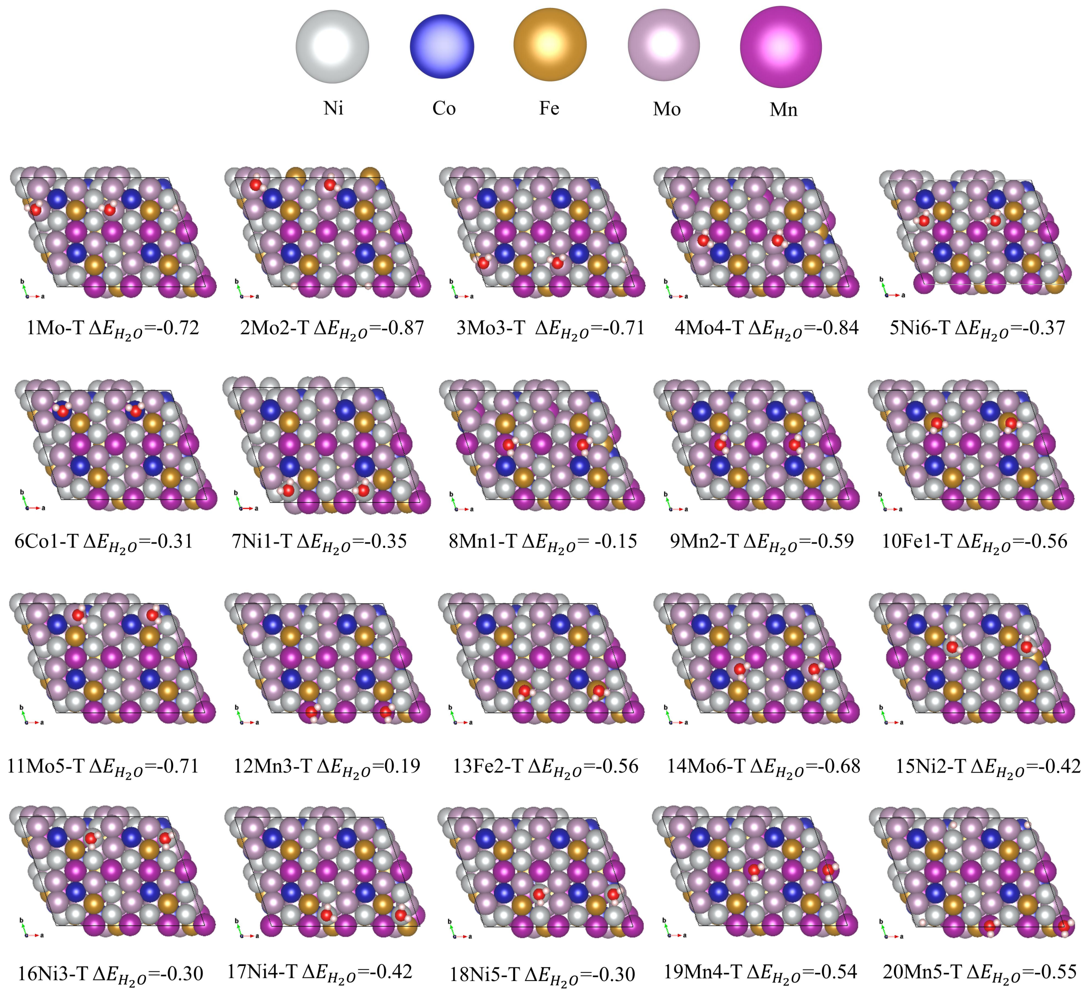

1Mo-T ΔE_{H_2O}=-0.72 2Mo2-T ΔE_{H_2O}=-0.87 3Mo3-T ΔE_{H_2O}=-0.71 4Mo4-T ΔE_{H_2O}=-0.84 5Ni6-T ΔE_{H_2O}=-0.37

6Co1-T ΔE_{H_2O}=-0.31 7Ni1-T ΔE_{H_2O}=-0.35 8Mn1-T ΔE_{H_2O}= -0.15 9Mn2-T ΔE_{H_2O}=-0.59 10Fe1-T ΔE_{H_2O}=-0.56

11Mo5-T ΔE_{H_2O}=-0.71 12Mn3-T ΔE_{H_2O}=0.19 13Fe2-T ΔE_{H_2O}=-0.56 14Mo6-T ΔE_{H_2O}=-0.68 15Ni2-T ΔE_{H_2O}=-0.42

16Ni3-T ΔE_{H_2O}=-0.30 17Ni4-T ΔE_{H_2O}=-0.42 18Ni5-T ΔE_{H_2O}=-0.30 19Mn4-T ΔE_{H_2O}=-0.54 20Mn5-T ΔE_{H_2O}=-0.55

Fig. S27 Local chemical environment of H_2O adsorption sites at HEA-(111) (un-SA) surfaces with various *ΔG*.

Table S1 Chemical compositions (at. %) of the NiCoFeMoMn alloy and np-NiCoFeMoMn 6h electrode as determined by SEM-EDS and XPSanalysis

element	NiCoFeMoMn	np-NiCoFeMoMn 6h	
		SEM-EDS	XPS
Ni	14.10	23.62	24.787
Co	14.38	11.82	14.361
Fe	14.30	8.86	13.685
Mo	6.02	30.73	24.216
Mn	51.19	24.98	22.951

Table S2 Chemical compositions (at. %) of the NiCoFeMoMn alloy and np-NiCoFeMoMn 6h electrode as determined by HADDF-STEM-EDS analysis

element	Total content	de-Total content	un-SA	de-un-SA	SA	de-SA
Ni	14.21	21.03	13.29	28.53	11.26	12.47
Co	14.3	14.39	15.22	12.61	16.60	17.28
Fe	14.33	12.53	15.09	9.60	13.59	13.71
Mo	5.82	24.52	4.94	30.71	11.29	16.95
Mn	51.45	27.53	51.46	18.55	47.25	39.59

Table S3 XPS analysis of the np-NiCoFeMoMn 6h electrode.

element	**Valence state**	**Orbit**	**Peak value**	**Peak area ratio (%)**	**Valence state ratio (%)**
Ni	0	2p 3/2	852.62	4.355	12.7
		2p 1/2	869.89	2.170	
	+2	2p 3/2	855.90	32.580	87.3
		2p 1/2	873.39	16.232	
	Sat.		861.49	29.427	
			879.23	15.236	
Co	0	2p 3/2	778.06	3.870	10.7
		2p 1/2	793.03	1.930	
	2+	2p 3/2	781.64	32.426	89.3
		2p 1/2	796.84	16.167	
	Sat.		785.54	24.777	
			802.77	20.829	
Fe	0	2p 3/2	707.10	8.671	14.7
		2p 1/2	720.20	4.337	
	2+	2p 3/2	710.70	25.438	85.3
		2p 1/2	724.30	12.725	
	Sat.		713.23	7.632	
			726.83	3.818	
	Co LMM		715.10	37.379	

Mo	0	3d 5/2	227.48	6.014	10.0
		3d 3/2	230.61	4.010	
	2+	3d 5/2	228.51	4.724	7.9
		3d 3/2	231.64	3.150	
	4+	3d 5/2	230.60	18.562	20.9
		3d 3/2	233.73	12.377	
	6+	3d 5/2	232.32	30.695	51.2
		3d 3/2	235.45	20.470	
Mn	0	2p 3/2	638.43	1.935	8.5
		2p 1/2	649.48	0.977	
	2+	2p 3/2	641.37	21.007	91.5
		2p 1/2	653.07	10.508	
	Sat.		646.99	3.760	
	Ni LMM		641.19	61.795	
O	2-		530.37	36.244	
	M-OH		531.51	59.750	
	H_2O		533.26	4.006	

Table S4 Comparisons of the HER catalytic activity of np-NiCoFeMoMn 6h electrode in 1 M KOH electrolyte

Electrocatalysts	Current density (mA cm^{-2})	Overpotential(mV)	Tafel slope (mV dec^{-1})	Refs.
np-NiCoFeMoMn 6h	10	14	29	This work
	100	49		
	1000	150		
CoNPs@C	100	260	106	12
NiO/Al_3Ni_2	100	140	42	13
Al-CoS_2 NWs	100	191	62.5	14
np-$Co_9S_4P_4$	100	174	51	15
FeCoNi-ATNs	100	200	40.2	16
Ni-Fe-P/NFx	100	150	74.5	17
Ni@NiFe	100	233	72.3	18
Co_3Mo/Cu	100	65	40	19
CoP|S	100	200	67	20
MoNi HM	100	380	36.6	21
NC/Ni_3Mo_3N/NF	100	136	41.5	22
$Ni_{40}Zr_{40}Ti_{20-x}Pt_x$ MG	100	70	30	23
(Ni-Fe)S_x/NiFe $(OH)_y$	100	124	68	24
Ni/$Mo_2C_{(1:2)}$-NCNFs	100	195	57.8	25
V-CoP@a-CeO_2	100	140	48.1	26
NiFeMoCoCr	100	281	41	27
Ni_5P_4-Ru	100	120	60	28
NiFeOx@NiCu	100	210	68	29
NiZn-CoO	100	160	47	30
$NiFeO_x$/CFP	100	220	31.5	31
$NiPt_3$@NiS/NF	100	73	24	32
NiFe-LDH/MXene/NF	100	200	70	33
NC/Vo-WON	100	76	33	34
NFP/C-3	100	125	54	35
RuSA-N-S-Ti_3C_2T	100	237	90	36
CoFeP TPAs/Ni	100	113	65.3	37
Ni_3S_2@MoS_2/FeOOH	100	177	85	38
Ni NWA	100	250	97	39
Co-Ni-S	100	190	43	40
Mo SAs	100	260	35.1	41
$Ni_{1.5}Co_{0.5}$@N-C NT/NF	100	270	117	42
CoP@NiFe-OH	100	180	71.7	43
CoMnP/Ni_2P/NiFe	100	250	58	44
$NiWO_4$/TM	100	140	51	45

Ni_5Co_3Mo-OH	100	260	59	[46]
Co_3Mo	100	180	61.3	[47]
TiO_2@Ni_3S_2	100	177	69	[48]
SANi-I	100	60	34.6	[49]
NiO/Ru@PNS	100	160	75	[50]
Ni(Cu)VO_x	100	130	28	[51]
$Ni_{1.8}Cu_{0.2}$-P	100	245	70	[52]

Table S5 Comparisons of the OER catalytic activity of np-NiCoFeMoMn 6h electrode in 1 M KOH electrolyte.

Electrocatalysts	Current density (mA cm^{-2})	Overpotential(mV)	Tafel slope (mV dec^{-1})	Refs.
np-NiCoFeMoMn 6h	10	243	37	This work
	100	284		
	1000	350		
FeCoNiAlTi	10	299	38	[53]
NiMoO4·xH2O/NF	150	403	46.7	[22]
AlNiCoIrMo	10	233	55.2	[54]
Co3Mo/Cu	164	367	82	[19]
SSW Rs-18 h	500	285	39	[55]
Ni/Mo2C-NCNFs	10	288	78.4	[25]
Fe-doped Co3O4	10	262	43	[56]
np-NiMnFeMo	10	265	65	[57]
CoSx@Cu2MoS4-MoS2/NSG	10	351	61.5	[58]
NiCo-HS@G	10	259	49.6	[59]

Table S6 Comparisons of the overall splitting water performance of np-NiCoFeMoMn 6h in alkaline electrolyte.

Electrocatalysts	Current density (mA cm^{-2})	Cell voltage (V)	Time (h)	Refs.
np-NiCoFeMoMn 6h	10	1.47	380	This work
NC/Ni3Mo3N/NF‖NiMoO4·xH2O/NF	10	1.58	50	22
AlNiCoIrMo	10	1.48	45	54
Co3Mo/Cu	145	1.65	30	19
SSW Rs-18 h	100	1.87	24	55
Ni/Mo2C-NCNFs	10	1.64	100	25
np-NiMnFeMo	10	1.57	20	57
CoSx@Cu2MoS4-MoS2/NSG	10	1.60	70	58
NiCo-HS@G	10	1.51	20	59
NiFeP	10	1.54	40	60
NiFeOx	10	1.63		61

References

1. van de Walle, A.; Asta, M.; Ceder, G., The alloy theoretic automated toolkit: A user guide. *Calphad* **2002,** *26* (4), 539-553.

2. van de Walle, A., Multicomponent multisublattice alloys, nonconfigurational entropy and other additions to the Alloy Theoretic Automated Toolkit. *Calphad* **2009,** *33* (2), 266-278.

3. Zhao, S.; Stocks, G. M.; Zhang, Y., Stacking fault energies of face-centered cubic concentrated solid solution alloys. *Acta Materialia* **2017,** *134*, 334-345.

4. Shang, S.-L.; Wang, Y.; Kim, D.; Liu, Z.-K., First-principles thermodynamics from phonon and Debye model: Application to Ni and Ni3Al. *Computational Materials Science* **2010,** *47* (4), 1040-1048.

5. Blochl, P. E., Projector augmented-wave method. *Phys Rev B Condens Matter* **1994,** *50* (24), 17953-17979.

6. Kresse, G.; Joubert, D., From ultrasoft pseudopotentials to the projector augmented-wave method. *Physical Review B* **1999,** *59* (3), 1758-1775.

7. John P. Perdew, K. B., * Matthias Ernzerhof, Generalized gradient approximation made simple. *PHYSICAL REVIEW LETTERS* **1996,** *77*, 3865.

8. Kresse, G.; Hafner, J., Ab initiomolecular dynamics for liquid metals. *Physical Review B* **1993,** *47* (1), 558-561.

9. Grimme, S.; Antony, J.; Ehrlich, S.; Krieg, H., A consistent and accurate ab initio parametrization of density functional dispersion correction (DFT-D) for the 94 elements H-Pu. *The Journal of Chemical Physics* **2010,** *132* (15).

10. Monkhorst, H. J.; Pack, J. D., Special points for Brillouin-zone integrations. *Physical Review B* **1976,** *13* (12), 5188-5192.

11. Nørskov, J. K.; Bligaard, T.; Logadottir, A.; Kitchin, J. R.; Chen, J. G.; Pandelov, S.; Stimming, U., Trends in the Exchange Current for Hydrogen Evolution. *Journal of The Electrochemical Society* **2005,** *152* (3).

12. Jin, Q.; Ren, B.; Li, D.; Cui, H.; Wang, C., Plasma-Assisted Synthesis of Self-Supporting Porous CoNPs@C Nanosheet as Efficient and Stable Bifunctional Electrocatalysts for Overall Water Splitting. *ACS Appl Mater Interfaces* **2017,** *9* (37), 31913-31921.

13. Zhou, Y.; Liu, H.; Zhu, S.; Liang, Y.; Wu, S.; Li, Z.; Cui, Z.; Chang, C.; Yang, X.; Inoue, A., Highly Efficient and Self-Standing Nanoporous NiO/Al3Ni2 Electrocatalyst for Hydrogen Evolution Reaction. *ACS Applied Energy Materials* **2019,** *2* (11), 7913-7922.

14. Wang, M.; Zhang, W.; Zhang, F.; Zhang, Z.; Tang, B.; Li, J.; Wang, X., Theoretical Expectation and Experimental Implementation of In Situ Al-Doped CoS2 Nanowires on Dealloying-Derived Nanoporous Intermetallic Substrate as an Efficient Electrocatalyst for Boosting Hydrogen Production. *ACS Catalysis* **2019,** *9* (2), 1489-1502.

15. Tan, Y.; Luo, M.; Liu, P.; Cheng, C.; Han, J.; Watanabe, K.; Chen, M., Three-Dimensional Nanoporous Co9S4P4 Pentlandite as a Bifunctional Electrocatalyst for Overall Neutral Water Splitting. *ACS Appl Mater Interfaces* **2019,** *11* (4), 3880-3888.

16. Zhang, Q.; Bedford, N. M.; Pan, J.; Lu, X.; Amal, R., A Fully Reversible Water Electrolyzer Cell Made Up from FeCoNi (Oxy)hydroxide Atomic Layers. *Advanced Energy Materials* **2019,** *9* (29).
17. Wang, K.; Sun, K.; Yu, T.; Liu, X.; Wang, G.; Jiang, L.; Xie, G., Facile synthesis of nanoporous Ni–Fe–P bifunctional catalysts with high performance for overall water splitting. *Journal of Materials Chemistry A* **2019,** *7* (6), 2518-2523.
18. Cai, Z.; Bu, X.; Wang, P.; Su, W.; Wei, R.; Ho, J. C.; Yang, J.; Wang, X., Simple and cost effective fabrication of 3D porous core–shell Ni nanochains@NiFe layered double hydroxide nanosheet bifunctional electrocatalysts for overall water splitting. *Journal of Materials Chemistry A* **2019,** *7* (38), 21722-21729.
19. Shi, H.; Zhou, Y. T.; Yao, R. Q.; Wan, W. B.; Ge, X.; Zhang, W.; Wen, Z.; Lang, X. Y.; Zheng, W. T.; Jiang, Q., Spontaneously separated intermetallic Co3Mo from nanoporous copper as versatile electrocatalysts for highly efficient water splitting. *Nat Commun* **2020,** *11* (1), 2940.
20. Hong, W.; Jian, C.; Wang, G.; He, X.; Li, J.; Cai, Q.; Wen, Z.; Liu, W., Self-supported nanoporous cobalt phosphosulfate electrodes for efficient hydrogen evolution reaction. *Applied Catalysis B: Environmental* **2019,** *251*, 213-219.
21. Yang, L.; Zeng, L.; Liu, H.; Deng, Y.; Zhou, Z.; Yu, J.; Liu, H.; Zhou, W., Hierarchical microsphere of MoNi porous nanosheets as electrocatalyst and cocatalyst for hydrogen evolution reaction. *Applied Catalysis B: Environmental* **2019,** *249*, 98-105.
22. Chen, Y.; Yu, J.; Jia, J.; Liu, F.; Zhang, Y.; Xiong, G.; Zhang, R.; Yang, R.; Sun, D.; Liu, H.; Zhou, W., Metallic Ni3Mo3N Porous Microrods with Abundant Catalytic Sites as Efficient Electrocatalyst for Large Current Density and Superstability of Hydrogen Evolution Reaction and Water Splitting. *Applied Catalysis B: Environmental* **2020,** *272*.
23. Li, R.; Liu, X.; Wu, R.; Wang, J.; Li, Z.; Chan, K. C.; Wang, H.; Wu, Y.; Lu, Z., Flexible Honeycombed Nanoporous/Glassy Hybrid for Efficient Electrocatalytic Hydrogen Generation. *Adv Mater* **2019,** *31* (49), e1904989.
24. Che, Q.; Li, Q.; Tan, Y.; Chen, X.; Xu, X.; Chen, Y., One-step controllable synthesis of amorphous (Ni-Fe)S /NiFe(OH) hollow microtube/sphere films as superior bifunctional electrocatalysts for quasi-industrial water splitting at large-current-density. *Applied Catalysis B: Environmental* **2019,** *246*, 337-348.
25. Li, M.; Zhu, Y.; Wang, H.; Wang, C.; Pinna, N.; Lu, X., Ni Strongly Coupled with Mo2C Encapsulated in Nitrogen-Doped Carbon Nanofibers as Robust Bifunctional Catalyst for Overall Water Splitting. *Advanced Energy Materials* **2019,** *9* (10).
26. Yang, L.; Liu, R.; Jiao, L., Electronic Redistribution: Construction and Modulation of Interface Engineering on CoP for Enhancing Overall Water Splitting. *Advanced Functional Materials* **2020,** *30* (14).
27. Zhang, G.; Ming, K.; Kang, J.; Huang, Q.; Zhang, Z.; Zheng, X.; Bi, X., High entropy alloy as a highly active and stable electrocatalyst for hydrogen evolution reaction. *Electrochimica Acta* **2018,** *279*, 19-23.

28. He, Q.; Tian, D.; Jiang, H.; Cao, D.; Wei, S.; Liu, D.; Song, P.; Lin, Y.; Song, L., Achieving Efficient Alkaline Hydrogen Evolution Reaction over a Ni5 P4 Catalyst Incorporating Single-Atomic Ru Sites. *Adv Mater* **2020,** *32* (11), e1906972.

29. Zhou, Y.; Wang, Z.; Pan, Z.; Liu, L.; Xi, J.; Luo, X.; Shen, Y., Exceptional Performance of Hierarchical Ni-Fe (hydr)oxide@NiCu Electrocatalysts for Water Splitting. *Adv Mater* **2019,** *31* (8), e1806769.

30. Ling, T.; Zhang, T.; Ge, B.; Han, L.; Zheng, L.; Lin, F.; Xu, Z.; Hu, W. B.; Du, X. W.; Davey, K.; Qiao, S. Z., Well-Dispersed Nickel- and Zinc-Tailored Electronic Structure of a Transition Metal Oxide for Highly Active Alkaline Hydrogen Evolution Reaction. *Adv Mater* **2019,** *31* (16), e1807771.

31. Teng, X.; Wang, J.; Ji, L.; Lv, Y.; Chen, Z., Ni nanotube array-based electrodes by electrochemical alloying and de-alloying for efficient water splitting. *Nanoscale* **2018,** *10* (19), 9276-9285.

32. Panda, C.; Menezes, P. W.; Yao, S.; Schmidt, J.; Walter, C.; Hausmann, J. N.; Driess, M., Boosting Electrocatalytic Hydrogen Evolution Activity with a NiPt3@NiS Heteronanostructure Evolved from a Molecular Nickel-Platinum Precursor. *J Am Chem Soc* **2019,** *141* (34), 13306-13310.

33. Yu, M.; Wang, Z.; Liu, J.; Sun, F.; Yang, P.; Qiu, J., A hierarchically porous and hydrophilic 3D nickel–iron/MXene electrode for accelerating oxygen and hydrogen evolution at high current densities. *Nano Energy* **2019,** *63*.

34. Zhang, B.; Hou, J.; Wu, Y.; Cao, S.; Li, Z.; Nie, X.; Gao, Z.; Sun, L., Tailoring Active Sites in Mesoporous Defect‐Rich NC/Vo‐WON Heterostructure Array for Superior Electrocatalytic Hydrogen Evolution. *Advanced Energy Materials* **2019,** *9* (12).

35. Lu, X. F.; Yu, L.; Lou, X. W., Highly crystalline Ni-doped FeP/carbon hollow nanorods as all-pH efficient and durable hydrogen evolving electrocatalysts. *Sci Adv* **2019,** *5* (2).

36. Ramalingam, V.; Varadhan, P.; Fu, H. C.; Kim, H.; Zhang, D.; Chen, S.; Song, L.; Ma, D.; Wang, Y.; Alshareef, H. N.; He, J. H., Heteroatom-Mediated Interactions between Ruthenium Single Atoms and an MXene Support for Efficient Hydrogen Evolution. *Adv Mater* **2019,** *31* (48), e1903841.

37. Zhang, L.; Wang, X.; Li, A.; Zheng, X.; Peng, L.; Huang, J.; Deng, Z.; Chen, H.; Wei, Z., Rational construction of macroporous CoFeP triangular plate arrays from bimetal–organic frameworks as high-performance overall water-splitting catalysts. *Journal of Materials Chemistry A* **2019,** *7* (29), 17529-17535.

38. Zheng, M.; Guo, K.; Jiang, W.-J.; Tang, T.; Wang, X.; Zhou, P.; Du, J.; Zhao, Y.; Xu, C.; Hu, J.-S., When MoS2 meets FeOOH: A “one-stone-two-birds” heterostructure as a bifunctional electrocatalyst for efficient alkaline water splitting. *Applied Catalysis B: Environmental* **2019,** *244*, 1004-1012.

39. Hsieh, C. T.; Chuah, X. F.; Huang, C. L.; Lin, H. W.; Chen, Y. A.; Lu, S. Y., NiFe/$(Ni,Fe)_3S_2$ Core/Shell Nanowire Arrays as Outstanding Catalysts for Electrolytic Water Splitting at High Current Densities. *Small Methods* **2019,** *3* (10).

40. Yin, J.; Jin, J.; Zhang, H.; Lu, M.; Peng, Y.; Huang, B.; Xi, P.; Yan, C.

H., Atomic Arrangement in Metal-Doped NiS2 Boosts the Hydrogen Evolution Reaction in Alkaline Media. *Angew Chem Int Ed Engl* **2019,** *58* (51), 18676-18682.

41. Luo, Y.; Zhang, S.; Pan, H.; Xiao, S.; Guo, Z.; Tang, L.; Khan, U.; Ding, B. F.; Li, M.; Cai, Z.; Zhao, Y.; Lv, W.; Feng, Q.; Zou, X.; Lin, J.; Cheng, H. M.; Liu, B., Unsaturated Single Atoms on Monolayer Transition Metal Dichalcogenides for Ultrafast Hydrogen Evolution. *ACS Nano* **2020,** *14* (1), 767-776.

42. Li, T.; Li, S.; Liu, Q.; Yin, J.; Sun, D.; Zhang, M.; Xu, L.; Tang, Y.; Zhang, Y., Immobilization of Ni3Co Nanoparticles into N-Doped Carbon Nanotube/Nanofiber Integrated Hierarchically Branched Architectures toward Efficient Overall Water Splitting. *Adv Sci (Weinh)* **2020,** *7* (1), 1902371.

43. Li, Y.; Guo, S.; Jin, T.; Wang, Y.; Cheng, F.; Jiao, L., Promoted synergy in core-branch CoP@NiFe–OH nanohybrids for efficient electrochemical-/photovoltage-driven overall water splitting. *Nano Energy* **2019,** *63*.

44. Bu, X.; Wei, R.; Gao, W.; Lan, C.; Ho, J. C., A unique sandwich structure of a CoMnP/Ni2P/NiFe electrocatalyst for highly efficient overall water splitting. *Journal of Materials Chemistry A* **2019,** *7* (19), 12325-12332.

45. Ji, Y.; Yang, L.; Ren, X.; Cui, G.; Xiong, X.; Sun, X., Full Water Splitting Electrocatalyzed by NiWO4 Nanowire Array. *ACS Sustainable Chemistry & Engineering* **2018,** *6* (8), 9555-9559.

46. Hao, S.; Chen, L.; Yu, C.; Yang, B.; Li, Z.; Hou, Y.; Lei, L.; Zhang, X., NiCoMo Hydroxide Nanosheet Arrays Synthesized via Chloride Corrosion for Overall Water Splitting. *ACS Energy Letters* **2019,** *4* (4), 952-959.

47. Chen, J.; Ge, Y.; Feng, Q.; Zhuang, P.; Chu, H.; Cao, Y.; Smith, W. R.; Dong, P.; Ye, M.; Shen, J., Nesting Co3Mo Binary Alloy Nanoparticles onto Molybdenum Oxide Nanosheet Arrays for Superior Hydrogen Evolution Reaction. *ACS Appl Mater Interfaces* **2019,** *11* (9), 9002-9010.

48. Deng, S.; Zhang, K.; Xie, D.; Zhang, Y.; Zhang, Y.; Wang, Y.; Wu, J.; Wang, X.; Fan, H. J.; Xia, X.; Tu, J., High-Index-Faceted Ni3S2 Branch Arrays as Bifunctional Electrocatalysts for Efficient Water Splitting. *Nano-Micro Letters* **2019,** *11* (1).

49. Zhao, Y.; Ling, T.; Chen, S.; Jin, B.; Vasileff, A.; Jiao, Y.; Song, L.; Luo, J.; Qiao, S. Z., Non-metal Single-Iodine-Atom Electrocatalysts for the Hydrogen Evolution Reaction. *Angew Chem Int Ed Engl* **2019,** *58* (35), 12252-12257.

50. Zhong, C.; Zhou, Q.; Li, S.; Cao, L.; Li, J.; Shen, Z.; Ma, H.; Liu, J.; Lu, M.; Zhang, H., Enhanced synergistic catalysis by a novel triple-phase interface design of NiO/Ru@Ni for the hydrogen evolution reaction. *Journal of Materials Chemistry A* **2019,** *7* (5), 2344-2350.

51. Li, Y.; Tan, X.; Hocking, R. K.; Bo, X.; Ren, H.; Johannessen, B.; Smith, S. C.; Zhao, C., Implanting Ni-O-VOx sites into Cu-doped Ni for low-overpotential alkaline hydrogen evolution. *Nat Commun* **2020,** *11* (1), 2720.

52. Chu, S.; Chen, W.; Chen, G.; Huang, J.; Zhang, R.; Song, C.; Wang, X.; Li, C.; Ostrikov, K., Holey Ni-Cu phosphide nanosheets as a highly efficient and stable electrocatalyst for hydrogen evolution. *Applied Catalysis B: Environmental* **2019,** *243*, 537-545.

53. Jia, Z.; Yang, T.; Sun, L.; Zhao, Y.; Li, W.; Luan, J.; Lyu, F.; Zhang, L. C.; Kruzic, J. J.; Kai, J. J.; Huang, J. C.; Lu, J.; Liu, C. T., A Novel Multinary Intermetallic as an Active Electrocatalyst for Hydrogen Evolution. *Adv Mater* **2020,** *32* (21), e2000385.
54. Jin, Z.; Lv, J.; Jia, H.; Liu, W.; Li, H.; Chen, Z.; Lin, X.; Xie, G.; Liu, X.; Sun, S.; Qiu, H. J., Nanoporous Al-Ni-Co-Ir-Mo High-Entropy Alloy for Record-High Water Splitting Activity in Acidic Environments. *Small* **2019,** *15* (47), e1904180.
55. Jothi, V. R.; Karuppasamy, K.; Maiyalagan, T.; Rajan, H.; Jung, C. Y.; Yi, S. C., Corrosion and Alloy Engineering in Rational Design of High Current Density Electrodes for Efficient Water Splitting. *Advanced Energy Materials* **2020,** *10* (24).
56. Zhang, S. L.; Guan, B. Y.; Lu, X. F.; Xi, S.; Du, Y.; Lou, X. W. D., Metal Atom-Doped Co3 O4 Hierarchical Nanoplates for Electrocatalytic Oxygen Evolution. *Adv Mater* **2020,** *32* (31), e2002235.
57. Liu, H.; Xi, C.; Xin, J.; Zhang, G.; Zhang, S.; Zhang, Z.; Huang, Q.; Li, J.; Liu, H.; Kang, J., Free-standing nanoporous NiMnFeMo alloy: An efficient non-precious metal electrocatalyst for water splitting. *Chemical Engineering Journal* **2021,** *404*.
58. Nguyen, D. C.; Tran, D. T.; Doan, T. L. L.; Kim, D. H.; Kim, N. H.; Lee, J. H., Rational Design of Core@shell Structured CoSx@Cu2MoS4 Hybridized MoS2/N,S‐Codoped Graphene as Advanced Electrocatalyst for Water Splitting and Zn‐Air Battery. *Advanced Energy Materials* **2020,** *10* (8).
59. Tang, T.; Jiang, W.-J.; Niu, S.; Liu, N.; Luo, H.; Zhang, Q.; Wen, W.; Chen, Y.-Y.; Huang, L.-B.; Gao, F.; Hu, J.-S., Kinetically Controlled Coprecipitation for General Fast Synthesis of Sandwiched Metal Hydroxide Nanosheets/Graphene Composites toward Efficient Water Splitting. *Advanced Functional Materials* **2018,** *28* (3).
60. Li, R.-Q.; Wang, B.-L.; Gao, T.; Zhang, R.; Xu, C.; Jiang, X.; Zeng, J.; Bando, Y.; Hu, P.; Li, Y.; Wang, X.-B., Monolithic electrode integrated of ultrathin NiFeP on 3D strutted graphene for bifunctionally efficient overall water splitting. *Nano Energy* **2019,** *58*, 870-876.
61. Yu, X.; Yu, Z.-Y.; Zhang, X.-L.; Li, P.; Sun, B.; Gao, X.; Yan, K.; Liu, H.; Duan, Y.; Gao, M.-R.; Wang, G.; Yu, S.-H., Highly disordered cobalt oxide nanostructure induced by sulfur incorporation for efficient overall water splitting. *Nano Energy* **2020,** *71*.